

Control of Natural Gas Catalytic Partial Oxidation for Hydrogen Generation in Fuel Cell Applications

Jay T. Pukrushpan, Anna G. Stefanopoulou, *Member, IEEE*, Subbarao Varigonda, *Member, IEEE*, Lars M. Pedersen, *Member, IEEE*, Shubhro Ghosh, and Hwei Peng

Abstract—A fuel processor that reforms natural gas to hydrogen-rich mixture to feed the anode field of fuel cell stack is considered. The first reactor that generates the majority of the hydrogen in the fuel processor is based on catalytic partial oxidation of the methane in the natural gas. We present a model-based control analysis and design for a fuel processing system (FPS) that manages natural gas flow and humidified atmospheric air flow in order to regulate 1) the amount of hydrogen in the fuel cell anode and 2) the temperature of the catalytic partial oxidation reactor during transient power demands from the fuel cell.

Linear feedback analysis and design is used to identify the limitation of a decentralized controller and the benefit of a multivariable controller. Further analysis unveils the critical controller cross coupling term that contributes to the superior performance of the multivariable controller.

Index Terms—Fuel cell, fuel processor, hydrogen generation, multivariable feedback, process modeling.

I. INTRODUCTION

FUEL CELLS are considered for stationary (residential and commercial) and mobile (automotive and portable) power generation due to their high efficiency and environmental friendliness. Inadequate infrastructure for hydrogen refueling, distribution, and storage makes the fuel processor technology an important part of the fuel cell system for both stationary and mobile applications. For residential applications, fueling the fuel cell system using natural gas is often preferred because of its wide availability and extended distribution system [1]. Common methods of converting natural gas to hydrogen include steam reforming and partial oxidation. The most common method, steam reforming is well suited for steady-state operation and can deliver a relatively high concentration of hydrogen [2], but it suffers from a poor transient operation [3]. On the other hand, the partial oxidation offers several other advantages such as compactness, rapid-startup, and responsiveness to load changes [1], but delivers lower conversion efficiency.

Manuscript received March 26, 2003; revised November 23, 2003. Manuscript received in final form March 23, 2004. Recommended by Associate Editor M. Jankovic. This work was supported in part by the National Science Foundation under Grant CMS-021332 and in part by grants from United Technologies.

J. T. Pukrushpan is with the Department of Mechanical Engineering, Kasetsart University, Chatuchak, Bangkok, 10900, Thailand (e-mail: fengjwp@ku.ac.th).

A. G. Stefanopoulou and H. Peng are with the Department of Mechanical Engineering, University of Michigan, Ann Arbor, MI 48109 USA (e-mail: hpeng@umich.edu).

S. Varigonda, L. M. Pedersen, and S. Ghosh are with the United Technologies Research Center, East Hartford, CT 06108 USA (e-mail: varigos@utrc.utcc.com; ghoshos@utrc.utcc.com).

Digital Object Identifier 10.1109/TCST.2004.833649

A schematic of a typical partial oxidation-based FPS is shown in Fig. 1. The majority of hydrogen is generated in a CPOX where natural gas (mostly methane CH_4) is combined with oxygen (in air) over a solid catalyst bed [4]. The two main factors that affect CH_4 to H_2 conversion efficiency of the CPOX are the catalyst bed temperature and the ratio of the reactants (CH_4 and O_2) [5]. At proper CPOX operating temperature, the amount of hydrogen created depends on the supply rate of CH_4 and the CPOX air to fuel ratio, more specifically, the oxygen to carbon ratio. This oxygen to carbon ratio also influences the amount of heat generated in the CPOX, which then affects the CPOX catalyst bed temperature. Carbon monoxide (CO), which poisons the fuel cell catalyst, is also created in the CPOX along with H_2 and, thus, additional processing is needed to remove the CO. The typical CO removal process involves two reactors: water gas shift (WGS) and preferential oxidation (PROX) [6], which are represented, in this paper, as if they perfectly remove the CO with the introduction of water and air. More details on the FPS chemical reactions are given in Section II.

During changes in the stack current, the fuel processor needs to 1) quickly regulate the amount of hydrogen in the fuel cell stack (anode) to avoid starvation or wasted hydrogen [7] and 2) maintain a desired temperature of the CPOX catalyst bed for high-conversion efficiency [8]. Accurate control and coordination of the fuel processor reactant flows can prevent both large deviation of hydrogen concentration in the anode and large excursion of CPOX catalyst bed temperature. A control-oriented nonlinear model of the natural gas FPS is developed in Section III with a focus on the dynamic behaviors associated with the flows and pressure in the FPS and also the temperature of the CPOX. The two main performance variables are the anode hydrogen mole fraction [9] and the CPOX catalyst bed temperature [5]. The two control actuators are the fuel (CH_4) valve command and the CPOX air blower command. The control problem is formulated in Section IV and a linearized model derived in Section V is used in the control analysis and design.

Typical FPS rely on a decentralized [single-input–single-output (SISO)] control of the air blower command to control CPOX temperature and of the fuel valve command to control the anode hydrogen concentration. In Section VI, an analysis using the relative gain array method confirms the appropriateness of the traditional input–output pairs for the decentralized control. The study also shows large interactions between the two loops at high frequencies and different operating conditions. These interactions can be more efficiently handled with multivariable control which is studied in Section VIII. The linear quadratic optimal control method is used to design the controller (LQR)

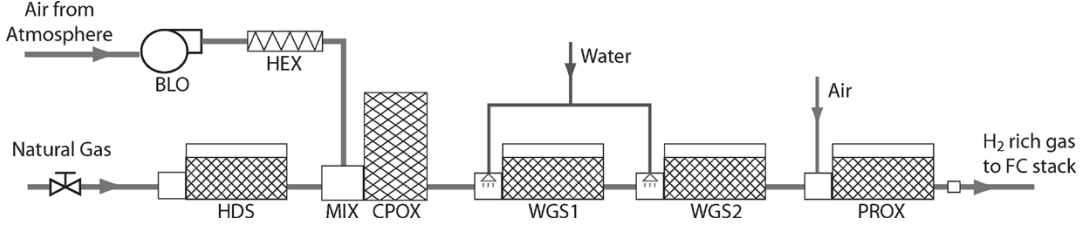
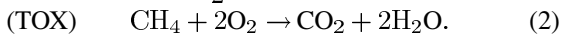
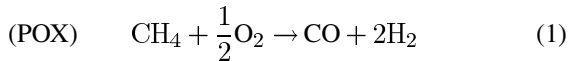


Fig. 1. FPS components.

and the state estimator (LQG) that achieves a significant improvement in the CPOX temperature regulation as compared to the decentralized controller. It is shown in Section IX that the regulation of the anode H_2 mole fraction depends strongly on the speed of the fuel valve command while the improvement in the CPOX temperature regulation is due to the coordination of both inputs.

II. FPS

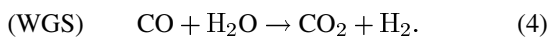
Fig. 1 illustrates the components in a natural gas FPS [10]. Natural gas (mostly methane CH_4) is supplied to the FPS from either a high-pressure tank or a high-pressure pipeline. The main air flow is supplied to the system by a blower (BLO) which draws air from the atmosphere. The air is then heated in the heat exchanger (HEX). The hydro-desulfurizer (HDS) is used to remove sulfur present in the natural gas stream [1], [11]. The desulfurized natural gas stream is then mixed with the heated air flow in the mixer (MIX). The mixture is then passed through the catalyst bed inside the CPOX where CH_4 reacts with oxygen to produce H_2 . There are two main chemical reactions taking place in the CPOX: partial oxidation (POX) and total oxidation (TOX) [5], [12]



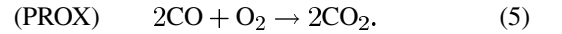
Heat is released from both reactions. However, TOX reaction releases more heat than POX reaction. The difference in the rates of the two reactions depends on the selectivity, S , defined as

$$S = \frac{\text{rate of } CH_4 \text{ reacting in POX}}{\text{total rate of } CH_4 \text{ reacting}}. \quad (3)$$

The selectivity depends strongly on the oxygen to carbon ratio (O_2 to CH_4), denoted by λ_{O_2C} , entering the CPOX [5]. Hydrogen is created only in POX reaction and, therefore, it is preferable to promote this reaction in the CPOX. However, the heat generated from POX reaction is not sufficient to maintain CPOX temperature. Thus, promoting TOX reaction is also required. CO is also created along with H_2 in the POX reaction as can be seen in (1). Since CO poisons the fuel cell catalyst, it is eliminated using both the WGS converter and the PROX. As illustrated in Fig. 1, there are typically two WGS reactors operating at different temperatures [3], [6]. In the WGS, water is injected into the gas flow in order to promote a water gas shift reaction



Note that even though the objective of WGS is to eliminate CO, hydrogen is also created from the WGS reaction. The level of CO in the gas stream after WGS is normally still high for fuel cell operation and, thus, oxygen is injected (in the form of air) into the PROX reactor to react with the remaining CO



The amount of air injected into the PROX is typically twice the amount that is needed to maintain the stoichiometric reaction in (5) [3], [13].

III. CONTROL-ORIENTED FPS MODEL

The FPS model is developed with a focus on the dynamic behaviors associated with the flows and pressures in the FPS and also the temperature of the CPOX [14], [15]. The focus of the control study is on H_2 generation and, thus, the model incorporates relatively more details of the CPOX reactor while using simple models for the WGS and PROX reactors, which function mainly for CO removal. The model is used to predict the effects of fuel and air flow command to CPOX temperature [5], stack H_2 concentration [16], and not CO concentration.

Several assumptions are made in order to simplify the FPS model. Since the control of WGS and PROX reactants are not studied, the two components are lumped together as one volume and the combined volume is called WROX (WGS+PROX). In this paper, we focus on H_2 generation, it is, thus, assumed that WGS and PROX, which are mainly used for CO removal, are perfectly controlled to obtain desired conversion and operating temperatures. Although control of WGS and PROX is a very challenging task, we assume its existence in this work because nonideal control will affect primarily the CO removal from the gas stream to the anode. Moreover, temperature deviations in the WROX subsystem do not affect significantly the upstream CPOX reactor. Conversely, the pressure dynamics of the WROX subsystem can influence the flow through the CPOX and, thus, pressure and flow interactions are captured in this model. Because the amount of H_2 created in WGS is proportional to the amount of CO that reacts in WGS [reaction (4)], which in turn, is proportional to the amount of H_2 generated in CPOX [reaction (1)], it is assumed that the amount of H_2 generated in the WGS is always a fixed percentage of the amount of H_2 produced in the CPOX. This assumption is consistent with the predictions from a detailed steady-state model [17]. A significantly more complex system model and thorough analysis is needed to fully understand the dynamic interactions between all the controlled reactors.

The desulfurization process in the HDS is not modeled and, thus, the HDS is viewed as a storage volume. It is assumed that

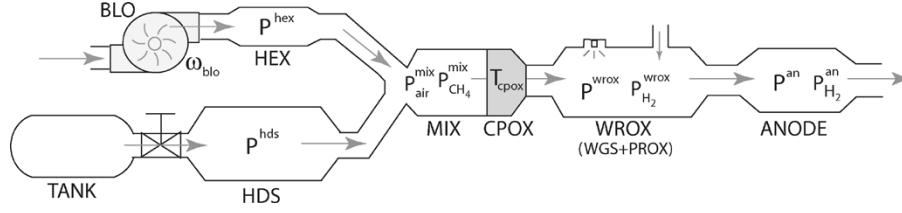


Fig. 2. FPS dynamic model.

the pressures and compositions of the air entering the blower and of the natural gas entering the HDS are constant. Natural gas is considered as pure methane CH_4 . Additionally, any temperature other than the CPOX temperature is assumed constant and the effect of temperature changes on the pressure dynamics is assumed negligible. The volume of CPOX is relatively small and its dynamics are captured in the mixer. It is also assumed that all reactions are fast and reach equilibrium before the flow exit the reactors. Finally, all gases obey the ideal gas law and all gas mixtures are perfect mixtures. Fig. 2 illustrates the simplified system and state variables used in the model.

The dynamic states in the model, also shown in Fig. 2, are blower speed ω_{blo} , heat exchanger pressure p^{hex} , HDS pressure p^{hds} , mixer CH_4 partial pressure $p_{\text{CH}_4}^{\text{mix}}$, mixer air partial pressure $p_{\text{air}}^{\text{mix}}$, CPOX temperature T_{cpox} , WROX (combined WGS and PROX) volume pressure p^{wrox} , WROX hydrogen partial pressure $p_{\text{H}_2}^{\text{wrox}}$, anode pressure p^{an} , and anode hydrogen partial pressure $p_{\text{H}_2}^{\text{an}}$. We provide here a brief outline of the model. The units used are pressure in Pascal, temperature in kelvin, and rotational speed in RPM. Although, we use the linearized model for the control analysis and design, the physical interpretation of the states helps in the control design and in interpreting the results.

The speed of the blower ω_{blo} is modeled as a first-order dynamic system with time constant τ_b . The governing equation is

$$\frac{d\omega_{\text{blo}}}{dt} = \frac{1}{\tau_b} \left(\frac{u_{\text{blo}}}{100} \omega_0 - \omega_{\text{blo}} \right) \quad (6)$$

where u_{blo} is the blower command signal (range between 0 and 100) and ω_0 is the maximum blower speed (3600 r/min). The gas flow rate through the blower is modeled, $\dot{W}_{\text{blo}} = f(\omega_{\text{blo}}, p_{\text{hex}}/p_{\text{atm}})$, using a blower map. Mass conservation with the ideal gas law through the isothermal assumption is used to model the pressure dynamics of the gas in all component volumes considered in the system. In any volume that does not involve any reaction, mixture composition is unchanged and the total pressure of the gas is used as the state (p_{hex} in HEX and p_{hds} in HDS). On the other hand, gas compositions in MIX, WROX, and fuel cell anode (AN) changes due to reactions involved. The changes in gas composition in these volumes are described with additional partial pressures of the important species. In general, the pressure dynamics of a gas n in a volume m is governed by

$$\frac{dp_n^m}{dt} = \frac{RT_m}{M_n V_m} (W_{n,\text{in}}^m - W_{n,\text{out}}^m) \quad (7)$$

where R is the universal gas constant, V_m is the component gas volume, M_n is the molar mass of species n , and T_m is the

temperature of the gas in the volume. The mass flow rate $W_{n,\text{in}}^m$ is the rate [in kilograms per second] of the species n going into the volume m which includes the species flow into the volume and the species produced (from the reaction) in the volume. The flow rate $W_{n,\text{out}}^m$ are the rate of species n going out of the volume including the species flow rate exiting the volume and the rate of species reacted in the reaction.

The total flow rate W between two volumes is, in general, calculated from pressure differential $p_1 - p_2$ using the orifice equation with a turbulent flow assumption

$$W = W_0 \sqrt{\frac{p_1 - p_2}{\Delta p_0}} \quad (8)$$

where W_0 and Δp_0 are the nominal air flow rate and the nominal pressure drop of the orifice, respectively. The flow rate of a constituent species n between the volumes is a function of the total gas flow and the mole fraction of the species n in the upstream volume. The flow rate of fuel (natural gas) into HDS $W_{\text{hds},\text{in}}$ is, in addition, a function of the valve input u_{valve}

$$W_{\text{hds},\text{in}} = \left(\frac{u_{\text{valve}}}{100} \right) W_{0,\text{valve}} \sqrt{\frac{p^{\text{tank}} - p^{\text{hds}}}{\Delta p_{0,\text{valve}}}} \quad (9)$$

where p^{tank} is the fuel tank or supply line pressure.

The conversion of the gases in CPOX is based on the reactions in (1) and (2) and the selectivity defined in (3), which is a function of the oxygen to carbon ratio in MIX, $\lambda_{\text{O}_2\text{C}}$

$$\lambda_{\text{O}_2\text{C}} = y_{\text{O}_2}^{\text{atm}} \frac{p_{\text{air}}^{\text{mix}}}{p_{\text{CH}_4}^{\text{mix}}} \quad (10)$$

where $y_{\text{O}_2}^{\text{atm}}$ is the oxygen mole fraction of the atmospheric air. The energy conservation principle is used to model the changes in CPOX temperature

$$m^{\text{cpx}} C_P^{\text{cpx}} \frac{dT_{\text{cpox}}}{dt} = \left[\begin{array}{c} \text{inlet} \\ \text{enthalpy} \\ \text{flow} \end{array} \right] - \left[\begin{array}{c} \text{outlet} \\ \text{enthalpy} \\ \text{flow} \end{array} \right] + \left[\begin{array}{c} \text{heat from} \\ \text{reactions} \end{array} \right] \quad (11)$$

where m^{cpx} (kg) and C_P^{cpx} (J/kg · K) are mass and specific heat capacity of the catalyst bed, respectively. The terms on the right hand side of (11) are determined based on the reactants and products gas of the CPOX reactions. Further details of the model are presented in [14].

IV. CONTROL PROBLEM FORMULATION

As previously discussed, the main objectives of the FPS controller are 1) to protect the stack from damage due to H_2 starvation; 2) to protect CPOX from overheating; and 3) to keep

overall system efficiency high, which includes high stack H_2 utilization and high FPS CH_4 -to- H_2 conversion. Objectives 2) and 3) are related since maintaining the desired CPOX temperature during steady-state implies proper regulation of the oxygen-to-carbon ratio which corresponds to high-FPS conversion efficiency.

Two performance variables that need to be regulated are the anode hydrogen mole fraction, y_{H_2}

$$y_{H_2} = \frac{p_{H_2}^{an}}{p^{an}} \quad (12)$$

calculated based on (7) and the CPOX temperature, T_{CPOX} , calculated based on (11). They are chosen based on the following rationale. High T_{CPOX} can cause the catalyst bed to be overheated and be permanently damaged. Low T_{CPOX} results in a low CH_4 reaction rate in the CPOX [5] and potential methane slip. Large deviations of y_{H_2} are undesirable. On one hand, a low value of y_{H_2} means anode H_2 starvation [9], [16], which can permanently damage the fuel cell structure. On the other hand, a high value of y_{H_2} means small hydrogen utilization which results in a waste of hydrogen.

In this control study, we assume that all CH_4 that enters the CPOX reacts without any methane slip. Note that these assumptions reduce the validity of the model for large T_{CPOX} deviations. The effect of the modeling error due to these assumptions can degrade the performance of the model-based controller. However, achieving one of the control goals, which is the regulation of T_{CPOX} , will ensure that this modeling error remains small.

The fuel valve actuator dynamics are ignored and we assume that u_{valve} in (9) is one of the two control signals. The second control signal is the blower command u_{blo} in (6). Note that the time constant τ_b captures the combined dynamics of the impeller inertia and the blower motor.

We assume that both performance variables are measured since regulation of the CPOX reactor temperature and the hydrogen exiting the fuel cell anode is a critical task. The temperature can be measured by a thermocouple or a noncontact temperature sensor [18]. The hydrogen mole fraction can be measured with a combination of electrochemical sensors [19], [20] and model-based observers [21]. An extensive research effort is currently underway to develop fast, repeatable, and robust hydrogen sensors. For example, a search performed in Oct. 2003 with keywords *hydrogen sensor* and *fuel cells* for patents filled in United States resulted in 53 relevant patents awarded and 36 patent applications published since March 2001. Motivated by this accelerating advances in hydrogen sensing technology we assume here perfect measurements of the performance variables. We discuss briefly the effects of this assumption on the system observability in Section VIII and in [15] and [22].

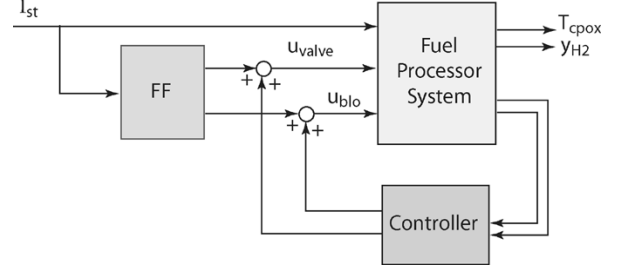


Fig. 3. Feedback control study.

The stack current I_{st} is considered as an exogenous input that is measured. Since the exogenous input is measured, we consider a two degree of freedom (2DOF) controller based on feedforward and feedback, as shown in Fig. 3. The feedforward terms that provide the valve and the blower signals that reject the steady-state effect of current to the outputs are integrated in the plant: $u^*(I_{st}) = [u_{blo}^*(I_{st}) \ u_{valve}^*(I_{st})]^T$. The value of u^* is obtained by nonlinear simulation and can be implemented with a lookup table. The performance variables are the CPOX temperature, T_{CPOX} , and the anode exit hydrogen mole fraction, y_{H_2} .

V. ANALYSIS OF LINEARIZED MODELS

A linear model of the FPS is obtained by linearizing the non-linear model. In this paper, the desired steady-state is selected at stack H_2 utilization $U_{H_2} = 80\%$ [13] and CPOX oxygen-to-carbon ratio $\lambda_{O_2C} = 0.6$. This condition results in the value of CPOX temperature, $T_{CPOX} = 972$ K (corresponds to $\lambda_{O_2C} = 0.6$), and the value of anode hydrogen mole fraction, $y_{H_2} = 8.8\%$ (corresponds to $U_{H_2} = 80\%$). The control objective is therefore to regulate T_{CPOX} at 972 K and y_{H_2} at 0.088. This desired value of T_{CPOX} also agrees with the value published in the literature [23]. Static feedforward terms (illustrated in Fig. 3) are included in the linear plant so that the steady-state T_{CPOX} and y_{H_2} are maintained at nominal value during changes in stack current. The linearization of the plant is denoted by

$$\begin{aligned} \dot{x} &= Ax + B_u u + B_w w \\ z &= C_z x + D_{zu} u + D_{zw} w \end{aligned} \quad (13)$$

where the state x , input u , disturbance w , and performance variables z are shown in the equation at the bottom of the page. The matrices in (13) are given in Table II. The linear model is scaled such that the units of the states are temperature in kelvin, pressure in kPa, and speed in kRPM. A similarity transformation (Pa to kPa and kRPM to kRPM) is used in the linearized system for better condition numbers. The input scaling is chosen to reflect the operating range for the inputs (u_{blo} and u_{valve} vary from 0% to 100%) and physical units are used for the current (I), and outputs (T_{CPOX} , y_{H_2}). Specifically, the current input is

$$\begin{aligned} x &= [T_{CPOX}, p_{H_2}^{an}, p^{an}, p^{hex}, \omega_{blo}, p^{hds}, p_{CH_4}^{mix}, p_{air}^{mix}, p_{H_2}^{wrox}, p^{wrox}]^T \\ w &= I_{st} \\ u &= [u_{blo} \ u_{valve}]^T \\ z &= [T_{CPOX} \ y_{H_2}]^T. \end{aligned}$$

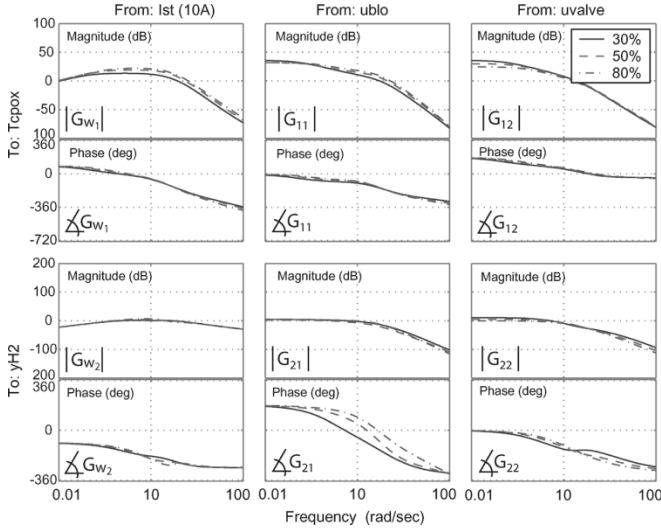


Fig. 4. Bode plot of linearized models at 30%, 50%, and 80% power.

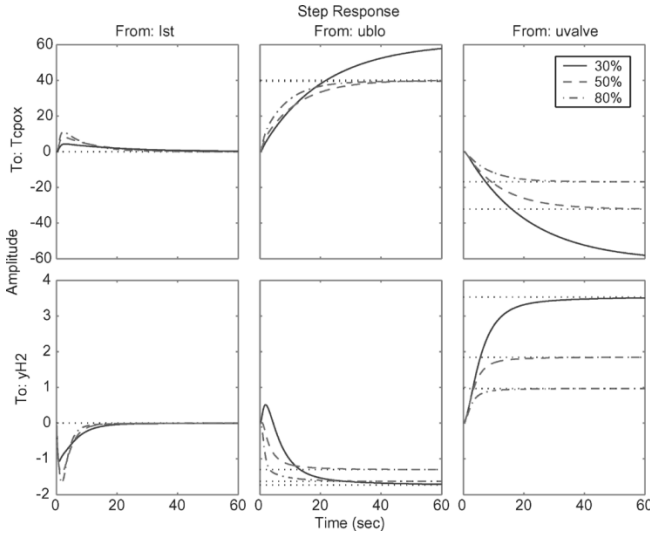


Fig. 5. Step responses of linearized models at 30%, 50%, and 80% power.

in ampere. The outputs are the CPOX temperature in kevin and the anode hydrogen mole fraction is in percent. All variables in the linear plant above are deviations from the nominal. In the transfer function form, we can represent the plant as

$$z = \begin{bmatrix} G_w & G \end{bmatrix} \begin{bmatrix} w \\ u \end{bmatrix}. \quad (14)$$

The nonlinear plant model is linearized at three different current (load) levels that correspond to the 30%, 50%, and 80% of the plant power level. The Bode plots and step responses of the linear plants that are obtained from different system power levels are shown in Figs. 4 and 5. For clarity, the units of current is ($\times 10$ A). Note first that the static feedforward controller does well in rejecting the effect from I_{st} to y_{H_2} and T_{cpx} in steady-state. The H_2 recovery using feedforward is, however, relatively slow. A feedback controller is, thus, needed to speed up the system behavior and to reduce the sensitivity introduced by modeling uncertainties.

The responses of the output due to step changes in the actuator signals, in Fig. 5, show a strongly coupled system. The fuel

 TABLE I
ABBREVIATIONS

Abbreviation	Meaning
BLO	Blower
CPOX	Catalytic Partial Oxidation
FPS	Fuel Processor System
HDS	Hydro-Desulfurizer
HEX	Heat Exchanger
LQ	Linear Quadratic
LQG	Linear Quadratic Gaussian
LQR	Linear Quadratic Regulator
MIMO	Multi-Input Multi-Output
MIX	Mixer
PID	Proportional, Integral and Derivative
PROX	Preferential Oxidation
RGA	Relative Gain Array
RHP	Right Half Plane
SISO	Single-Input Single Output
WGS	Water Gas Shift
WROX	WGS+PROX

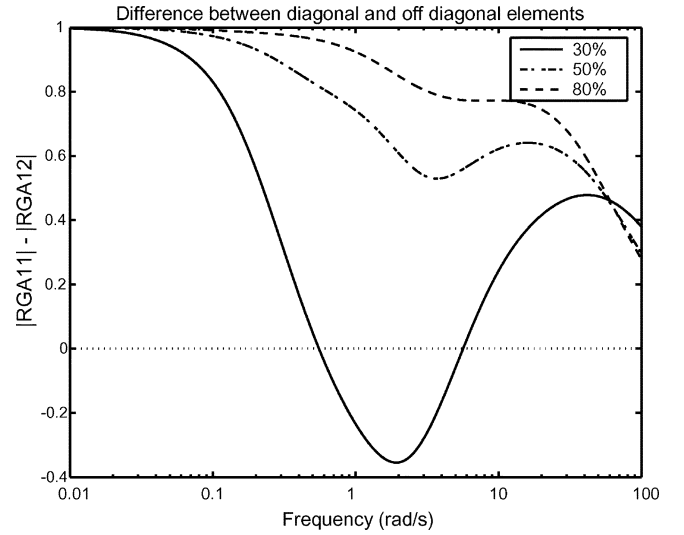


Fig. 6. Difference between diagonal and off-diagonal elements of the RGA matrix at different frequencies for three power setpoints.

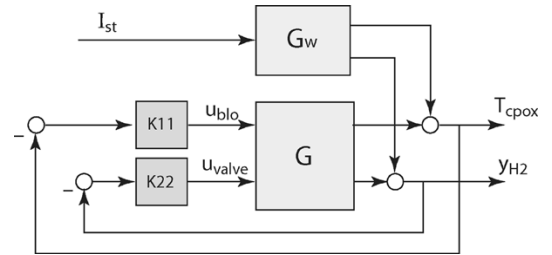


Fig. 7. Decentralized control.

dynamics are slower than the air dynamics, primarily due to the large HDS volume. Note that a right half plane (RHP) zero exists in the path $u_{blo} \rightarrow y_{H_2}$ can be easily detected from the initial inverse response of the y_{H_2} due to a step change in u_{blo} . Moreover, as can be seen in the step responses from u_{blo} to y_{H_2} , the RHP zero that causes the nonminimum phase behavior moves closer to the imaginary axis and causes larger initial inverse response at low-power level (30%). The linearization of the system at the 50% power level is used in the control study in the following sections.

TABLE II
FPS LINEAR MODEL SYSTEM MATRICES

A										Bu		Bw	
-0.074	0	0	0	0	0	-3.53	1.0748	0	1E-06	0	0	0	0
0	-1.468	-25.3	0	0	0	0	0	2.5582	13.911	0	0	-0.328	-0.024
0	0	-156	0	0	0	0	0	0	33.586	0	0	0	0
0	0	0	-124.5	212.63	0	112.69	112.69	0	0	0.12	0	0.0265	0.0504
0	0	0	0	-3.333	0	0	0	0	0	0	0.1834	0	0
0	0	0	0	0	-32.43	32.304	32.304	0	0	0	0	0	0
0	0	0	0	0	331.8	-344	-341	0	9.9042	0	0	0	0
0	0	0	221.97	0	0	-253.2	-254.9	0	32.526	0	0	0	0
0	0	2.0354	0	0	0	1.8309	1.214	-0.358	-3.304	0	0	0	0
0.0188	0	8.1642	0	0	0	5.6043	5.3994	0	-13.61	0	0	0	0
Cz										Dzu		Dzw	
1	0	0	0	0	0	0	0	0	0	0	0	0	0
0	0.994	-0.088	0	0	0	0	0	0	0	0	0	0	0

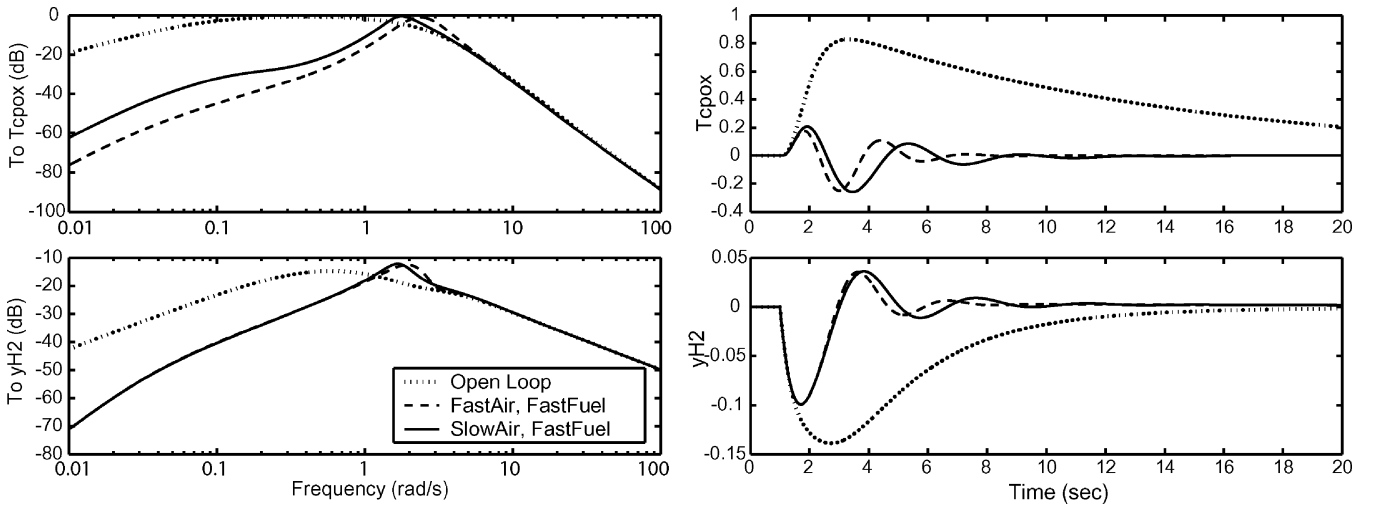


Fig. 8. Bode magnitude and unit step response of model at 50% power.

VI. INPUT-OUTPUT PAIRING

One of the most common approaches to controlling a multi-input-multi-output (MIMO) system is to use a diagonal controller, which is often referred to as a decentralized controller. The decentralized control works well if the plant is close to diagonal which means that the plant can be considered as a collection of individual SISO subplants with no interaction among them. In this case, the controller for each subplant can be designed independently. If the interaction between the loops is large, then the performance of the decentralized controller may be poor.

Due to the nonminimum phase (NMP) zero in the $u_{\text{blo}} \rightarrow y_{\text{H}_2}$ transfer function, the preferred pairing choices are $u_{\text{blo}} \rightarrow T_{\text{cpox}}$ pair and $u_{\text{valve}} \rightarrow y_{\text{H}_2}$ pair. This pairing choice is also confirmed by the relative gain array (RGA) matrix [24] of G

$$\text{RGA} = G \times (G^{-1})^T \quad (15)$$

which at zero frequency has negative off-diagonal elements

$$\text{RGA} \left(0 \frac{\text{rad}}{\text{s}} \right) = \begin{bmatrix} 2.302 & -1.302 \\ -1.302 & 2.302 \end{bmatrix}. \quad (16)$$

The RGA can also be used to assess the loop interactions. Large off-diagonal elements of the RGA matrix indicates large loop interactions. A plot of the magnitude difference between

the diagonal and off-diagonal elements of the RGA matrices in Fig. 6 shows that the interactions increase at high frequencies. At low power levels, the values of the off-diagonal elements of the RGA matrix are even higher than the diagonal elements ($|\text{RGA}_{11}| - |\text{RGA}_{12}| < 0$), indicating large coupling. At these frequencies, we can expect poor performance from a decentralized controller.

VII. DECENTRALIZED CONTROL

To illustrate the effect of the interactions, we design several PI controllers for the two SISO systems that correspond to the diagonal subsystem of G , i.e., $u_{\text{blo}} \rightarrow T_{\text{cpox}}(G(1,1))$, and $u_{\text{valve}} \rightarrow y_{\text{H}_2}(G(2,2))$. The diagram in Fig. 7 shows the decentralized controller.

The gains of the PI controllers K11 and K22 are chosen after iterations to achieve the best performance subject to actuator activity. Since a fast response of y_{H_2} is more critical, the PI controller in the fuel loop ($u_{\text{valve}} \rightarrow y_{\text{H}_2}$) is tuned first to achieve fast response of y_{H_2} without saturating the valve. Then, to achieve a fast regulation of T_{cpox} , we also tune the second PI for fast air loop while avoiding blower saturation. Fig. 8 shows the response using fast controllers in both loops in dashed line, for the system at medium power (50%). Due to the large

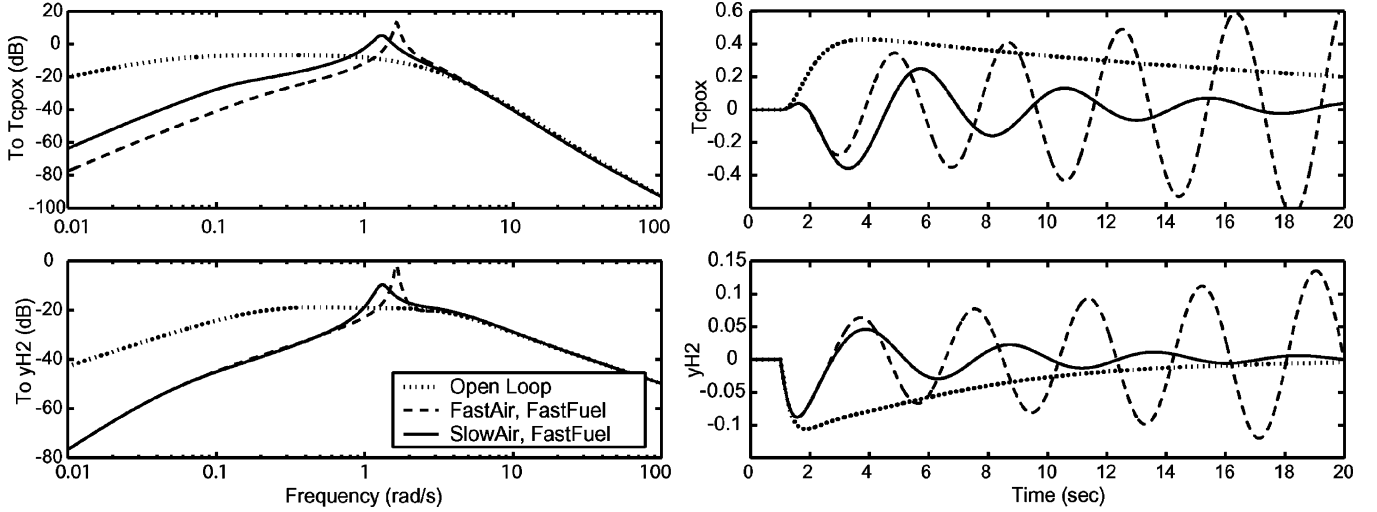


Fig. 9. Bode magnitude and unit step response of model at 30% power.

 TABLE III
 DECENTRALIZED PI CONTROLLERS

Controller	Transfer Function
K11	$0.0135 \frac{(5.6s + 1)}{s}$
K22	$0.165 \frac{(21s + 1)}{s}$

interaction as RGA predicted, the performance of the decentralized controller with fast controller in both loops degrades significantly when the system operate at low power as shown in Fig. 9. One way to compensate for the interaction is to create a bandwidth separation between the two loops. Since designing the air loop to be faster than the fuel loop is not feasible with a PI controller due to blower magnitude constraints, the air loop is detuned to be slower than the fuel loop. Figs. 8 and 9 also show the performance of the decentralized controller that has bandwidth separation. It can be seen that the speed of T_{cpox} regulation has to be sacrificed to prevent the degradation effect of the system interactions on the decentralized controller. The PI controllers chosen are given in Table III.

Note that more complex decentralized controllers can be used (high-order or PID, for example). The PI controller tuning here is used only to illustrate the effect of plant interactions and difficulties in tuning the PI controllers without systematic MIMO control tools. The conclusion from this section is that the large plant interactions illustrated by Fig. 6 must be considered in the control design.

An interesting point is that, for the decentralized PI controller, the bandwidth of the air loop needs to be smaller than the bandwidth of the fuel loop. This was the only way to achieve a bandwidth separation within the blower saturation constraints. However, if a higher order controller is allowed, a higher closed-loop bandwidth can be achieved. Indeed, as we show later in Section IX, a high-order decentralized controller using the diagonal

terms of a full MIMO controller achieves a decade higher bandwidth than the fuel loop without saturating the blower.

VIII. MULTIVARIABLE CONTROL

The previous section shows that the interactions in the plant limit the performance of the decentralized controller. In this section, we assess the improvement gained by a controller developed using a multivariable and model-based control design techniques. The controller is designed using linear quadratic (LQ) methodology.

To eliminate steady-state error, we add to the controller the integrators on the two performance variables, T_{cpox} and y_{H_2} . Note that, we assume that these two variables can be directly and instantaneously measured. The state equations of the integrators are

$$\frac{d}{dt} \begin{bmatrix} q_1 \\ q_2 \end{bmatrix} = \begin{bmatrix} T_{cpox}^{ref} - T_{cpox} \\ y_{H_2}^{ref} - y_{H_2} \end{bmatrix} \quad (17)$$

where $T_{cpox}^{ref} = 972$ K and $y_{H_2}^{ref} = 8.8\%$ are the desired values of T_{cpox} and y_{H_2} , respectively. In the linear domain, the desired deviation from the reference values is, thus, zero for all current commands. The controller is designed with the objective of minimizing the cost function

$$J = \int_0^{\infty} z^T Q_z z + q^T Q_I q + u^T R u dt \quad (18)$$

where Q_z , Q_I , and R are weighting matrices on the performance variables z , integrator state q , and control input u , respectively.

The control law that minimizes (18) is in the form

$$u = -K_P(\hat{x} - x_d) - K_I q = -K \begin{bmatrix} \hat{x} - x_d \\ q \end{bmatrix} \quad (19)$$

where K is the control gain and \hat{x} is the estimate of plant state. The values of K_P and K_I are given in Table IV. Variable x_d in (19) is a function of I_{st} and can be viewed as the desired values of the states that give the desired value of $z = 0$. In other words, the term $K_P x_d$ is an additional feedforward term that

TABLE IV
FPS CONTROLLER GAINS

K_p									
1.4054	0.18237	0.02904	1.0661	39.04	-6.6114	-0.70528	0.60367	0.76664	0.93881
-0.13028	1.1503	-0.13157	-0.24436	-8.422	6.1105	0.61755	-0.13879	3.787	0.12691
K_I									
-1.2071	-0.16911								
0.18907	-0.89972								
L									
469.67	138.59								
5.6245	818.34								
-93.622	-12.759								
-742.29	-99.077								
-30.245	-4.7928								
-795.89	-104.2								
-2149.2	-392.69								
1400.7	294.09								
1559.8	3547.1								
-430.89	-58.728								

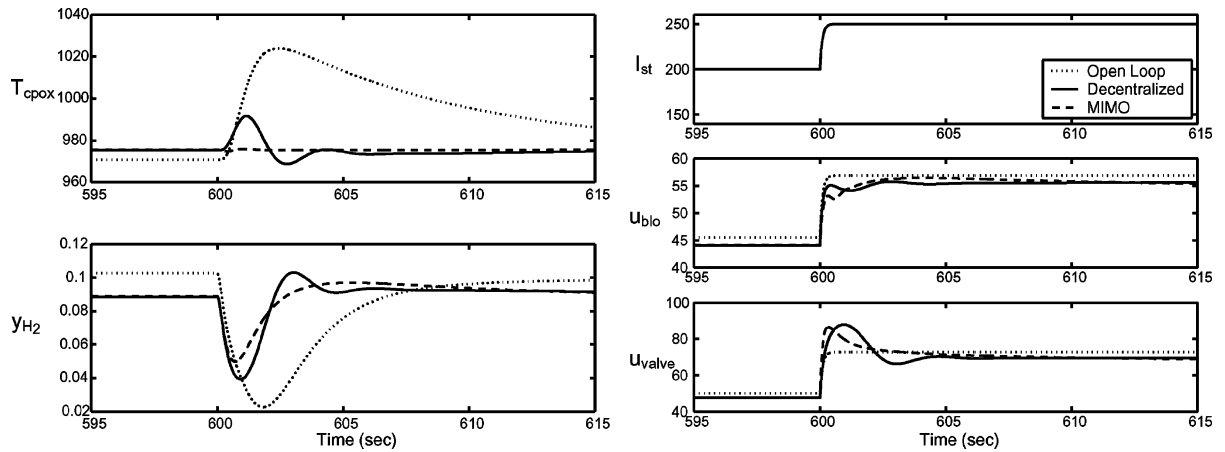


Fig. 10. Comparison of decentralized PI controller and observer feedback in nonlinear simulation. The lower left plot shows the actual fraction y_{H_2} and not the percent y_{H_2} as in all linear simulations.

compensates for the changes in the output steady-state value due to the feedback. As a result, this additional feedforward term is a function of the feedback gain K_p . The value of x_d can be found by simulation or by the linear plant matrices (13). As it is based on the linear model, the value of x_d calculated will be different from the actual desired state in the nonlinear plant. The error in x_d definitely influences the steady-state error of the performance variables, T_{cpox} and y_{H_2} . The integral control implemented through the augmented integrators (17) then becomes more critical. The fact that x_d is not accurate must be taken into account when choosing the weighting between Q_z and Q_I . Large integrator gain slows down the response, thus, relatively small Q_I shows a better (faster) performance in linear design. However, the response in nonlinear simulation with small Q_I gives poor steady-state performance since the performance is based heavily on the proportional part of the controller and therefore suffers from the error in x_d . Thus, if a more accurate value of x_d cannot be obtained, the transient performance must be compromised in order to get satis-

factory steady-state performance of the controller through the integral part. Alternatively, a more accurate x_d can be obtained by numerically solving the nonlinear simulation and stored in a lookup table.

The estimate of the plant state, \hat{x} , can be determined using the dynamic model of the plant together with the available performance measurements. The observer state equations are

$$\begin{aligned}\dot{\hat{x}} &= A\hat{x} + B_u u + B_w w + L(z - \hat{z}) \\ \hat{z} &= C_z \hat{x} + D_{zu} u + D_{zw} w\end{aligned}\quad (20)$$

where \hat{x} is the estimator state vector and L is the estimator gain (Table IV) determined based on LQG methodology. Analysis of the system observability in [14] reveals weakly observable modes and eventually leads to the design of a reduced order observer. Sensor lags typical in temperature and concentration measurements will degrade the system observability and, thus, the estimator performance [22]. The study in [15] shows that additional measurements, such as anode pressure p^{an} , improve the system observability. More work is, thus, needed to define

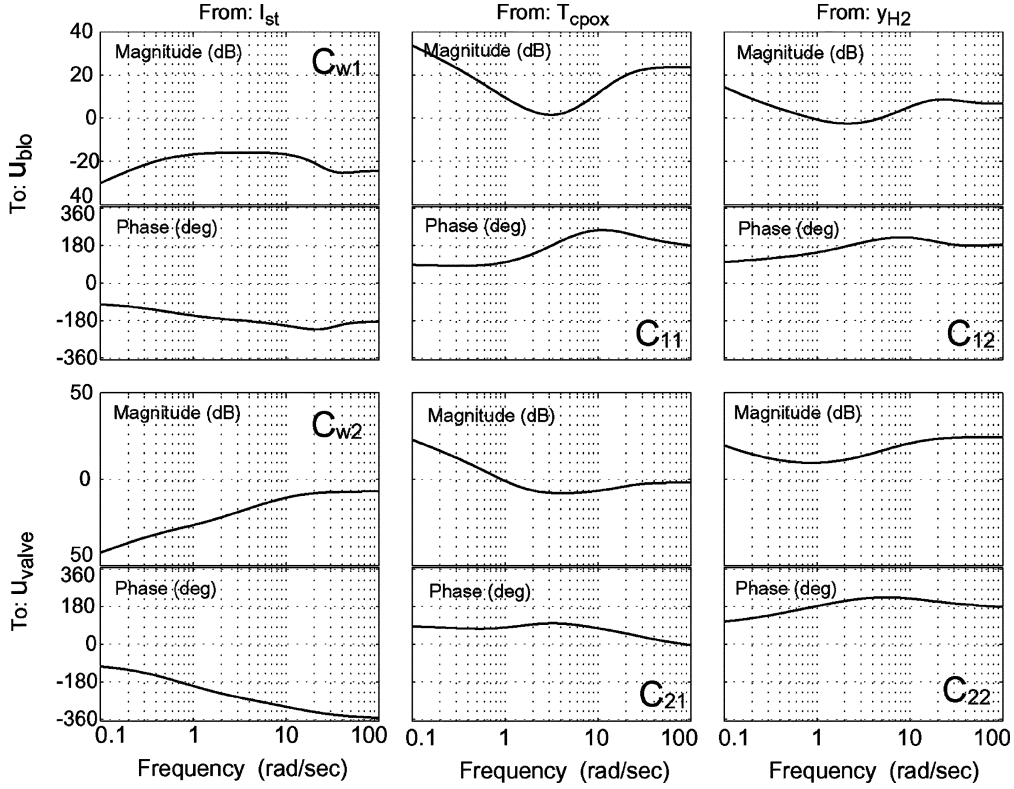


Fig. 11. Frequency response of the controller.

the measurements that will be beneficial for robust prevention of hydrogen starvation during fast load changes and low cost (slow) hydrogen sensing. Here, the assumption that both performance variables can be perfectly measured are used in order for us to determine the fundamental limitations or issues related to the plant based on the actuator topology and not the sensors.

The nonlinear simulation of the system with the decentralized PI feedback and with the output observer-based feedback is shown in Fig. 10. Note that to evaluate the closed-loop behavior of the nonlinear plant, current increases by 50 A and the lower left plot shows the actual fraction y_{H_2} . The output feedback gives satisfactory performance in both y_{H_2} and T_{cpox} regulations.

IX. INSIGHT GAINED BY THE MULTIVARIABLE DESIGN

The combination of the state feedback control (19) and the state observer (20) results in a model-based multivariable output-feedback controller. In transfer function form, the controller can be written as

$$u = C_w w + Cz = \begin{bmatrix} C_{w1} \\ C_{w2} \end{bmatrix} w + \begin{bmatrix} C_{11} & C_{12} \\ C_{21} & C_{22} \end{bmatrix} z. \quad (21)$$

The Bode plot of each element of the controller is shown in Fig. 11.

In an effort to simplify the feedback controller for gain scheduling and implementation purposes, we investigate which cross coupling term of the feedback contributes to the improvement by the MIMO controller. By zeroing out the cross coupling term and plotting the closed-loop frequency and time responses in Figs. 12 and 13, we can see that the performance of the full

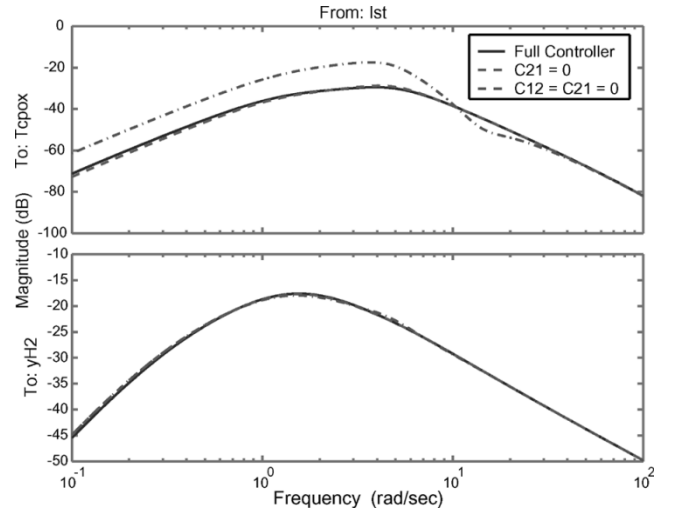


Fig. 12. Closed-loop frequency response for analysis of elements in the feedback controllers.

controller is maintained when $C_{21} = 0$ (triangular MIMO controller). However, the performance degrades when $C_{12} = 0$ (diagonal MIMO controller). Thus it is clear that the C_{12} term is the critical cross coupling term that provides the MIMO control improvement. This analysis gives a different result, however, if the air loop bandwidth is allowed to be higher, for example, by using a more powerful and faster blower. We can then lower the LQ weight on u_{blo} in the state feedback design. There is more actuator activity (high-bandwidth controller) of u_{blo} and the diagonal controller ($C_{12} = C_{21} = 0$) performs similarly to the full multivariable controller.

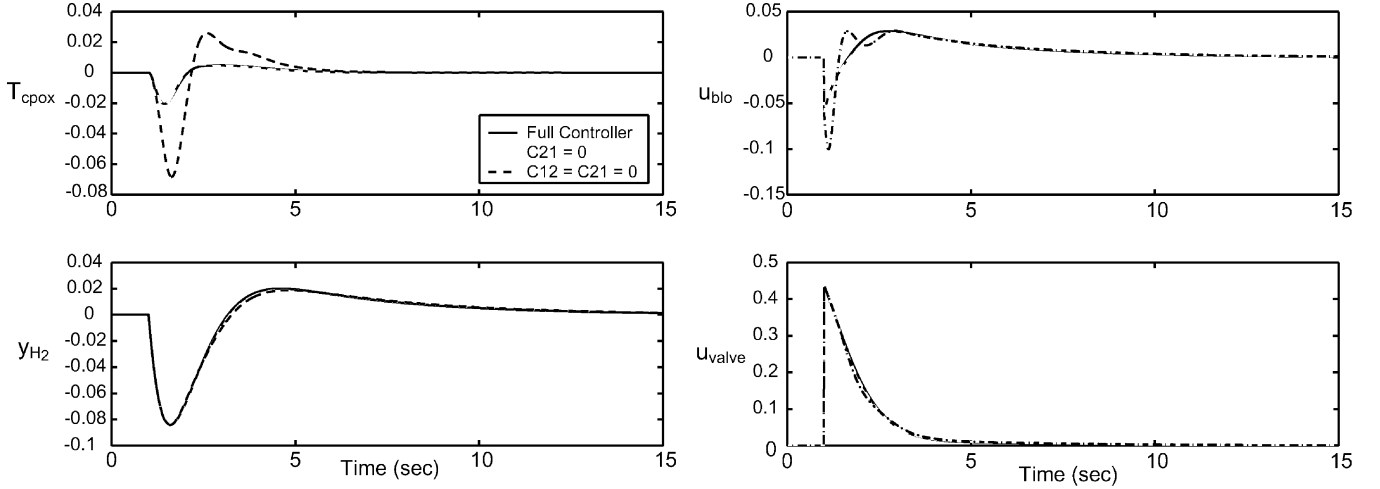


Fig. 13. Closed-loop time response for analysis of elements in the feedback controllers.

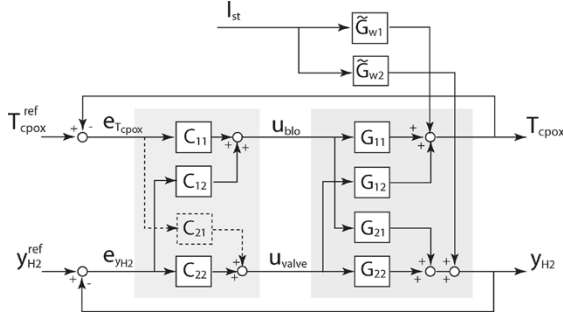


Fig. 14. Block diagram of FPS plant and simplified controller.

The importance of C_{12} is interpreted as follows. Following Fig. 14, the current disturbance, I_{st} , affects more y_{H_2} than T_{cpox} during fast transient as can be seen by the large high-frequency magnitude of the transfer function from I_{st} to y_{H_2} (Fig. 15) for the plant with feedforward control: $\tilde{G}_w = G_w + GC_w$. The valve signal, u_{valve} , tries to reject the effect of $\tilde{G}_{w2}I_{st}$ to y_{H_2} (see Fig. 14) by using the feedback C_{22} term through G_{22} . The blower signal, on the other hand, cannot reject the $\tilde{G}_{w2}I_{st}$ to y_{H_2} through $G_{21}C_{12}$ because of the nonminimum phase zero of G_{21} ($z_{NMP} = 3.07$). This can be verified by the equality of two frequency plots close to the nonminimum phase frequency

$$\frac{\tilde{G}_{w2}I_{st}}{1 + G_{21}C_{12} + G_{22}C_{22}} \approx \frac{\tilde{G}_{w2}I_{st}}{1 + G_{22}C_{22}}.$$

Indeed, Fig. 11 shows that the magnitude of C_{12} is low at frequencies close to that of the NMP zero. Meanwhile, the valve that tries hard to reject the $\tilde{G}_{w2}I_{st}$ to y_{H_2} causes disturbances to T_{cpox} through the plant G_{12} interaction. The controller cross coupling term C_{12} is, thus, needed to compensate for the effect of u_{valve} to T_{cpox} by partially cancelling $G_{12}C_{22}$ by $G_{11}C_{12}$ at certain frequencies.

$$T_{cpox} = \frac{G_{12}C_{22} + G_{11}C_{12}}{1 + G_{11}C_{11}} e_{y_{H_2}} \approx 0 \Rightarrow C_{12} \approx -G_{11}^{-1}G_{12}C_{22}.$$

Note that this partial cancellation involves the plant elements G_{11} and G_{12} that do not change significantly for different power levels, as compared to G_{21} (see Fig. 4). Thus, the benefit of the controller cross coupling term C_{12} is maintained in full range of

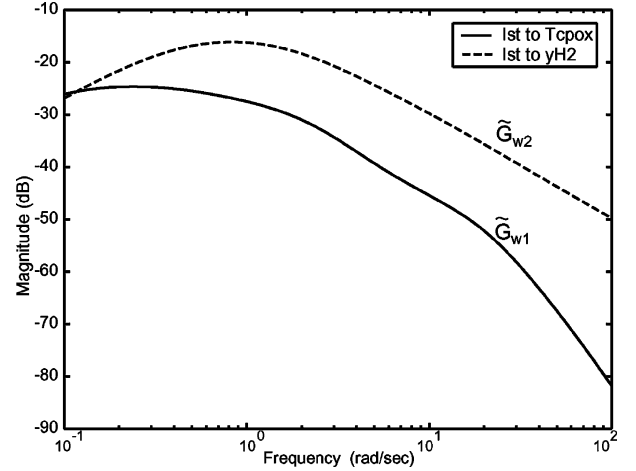


Fig. 15. Frequency magnitude plot of the plant with dynamic feedforward part of the controller \tilde{G}_{zw} .

operating power. If the air loop has high bandwidth, the $G_{11}C_{11}$ term can reject the disturbance by itself and, then, controller C_{12} is not needed to cancel the interaction from the valve to T_{cpox} .

Fig. 11 also verifies that C_{21} does not contribute to the overall MIMO controller. The magnitude of C_{21} is, in fact, relatively smaller than other feedback terms. At high frequencies where the effect of $\tilde{G}_{w2}I_{st}$ to y_{H_2} is large, the term C_{21} is not used to help regulating y_{H_2} because the deviation in y_{H_2} is not reflected in T_{cpox} measurement ($\tilde{G}_{w1}I_{st}$ is small). At low frequencies where I_{st} affects T_{cpox} , C_{21} may be used to help reduce T_{cpox} error but will cause disturbance to the well-behaved fuel loop, thus, C_{21} is also insignificant at low frequencies.

By comparing the response of decentralized PI controller in Fig. 10 and that of the diagonal MIMO controller in Fig. 13, we can see that the diagonal controller derived from the MIMO controller outperforms the decentralized PI controller. This is achieved as shown in Fig. 16 because of the higher closed-loop bandwidth of the air loop when compared with the one of the PI-based controller. As seen in Fig. 11, the high-order C_{11} term can have high bandwidth without having high gain and, thus, avoids blower saturation. This cannot be achieved using a PI controller. Indeed, Fig. 11 verifies that the gain of C_{11} is low

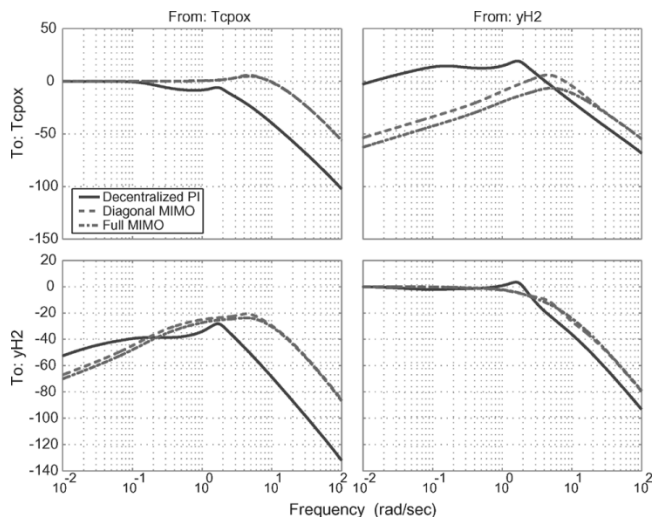


Fig. 16. Frequency (magnitude in decibels) response from reference signal of closed-loop system with MIMO controller.

at the frequencies where loop-interaction is large (see Fig. 6 for the loop interactions).

In summary, the MIMO controller achieves a superior performance in comparison with the decentralized PI controller due to two factors. First, the MIMO controller achieves a high bandwidth on the air loop without saturating the actuator by achieving high bandwidth without high gain. This is only feasible with high-order controllers. In hindsight of the success of the C_{11} term of the MIMO controller, one can design a PID or a PI + lead-lag controller that reproduces similar gain and phase to be used in the decentralized controller.

Second, the MIMO controller achieves better coordination between the two actuators by utilizing a cross coupling term. The cross coupling term acts in a “feedforward” sense and changes the blower command based on how the fuel valve behaves. This partially cancels the interaction between the fuel valve to the air loop. This partial cancellation, luckily, involves plant elements that do not change significantly for different power levels. Thus, without having explicitly designed for robustness, the MIMO controller maintains its performance at all power levels.

X. CONCLUSION

The control problem of hydrogen generation using catalytic partial oxidation and prevention of fuel cell stack starvation is studied. The two-input two-output control problem has the air blower and the fuel valve as inputs and the CPOX temperature and the anode hydrogen mole fraction (anode starvation) as performance variables.

We show that tuning two PI controllers for the air and the fuel loops is difficult. Moreover, the closed-loop performance is adversely affected by the intrinsic interaction between the two loops. One way to prevent the performance degradation is to have bandwidth separation between the two control loops. This introduces a compromise of the air-temperature closed-loop response in favor to the fuel-hydrogen loop.

On the other hand, a model-based high-order controller designed using linear multivariable methodologies, LQR-LQG in our case, can achieve very good response for a wide range of

operating conditions. Our analysis shows that the multivariable controller can be simplified to a lower triangular controller where the blower command depends on both errors in T_{CPOX} and y_{H_2} (or, equivalently, fuel valve). If the multivariable controller is further simplified to a diagonal controller (no cross coupling between control inputs and errors in the performance variables), the closed-loop performance degrades with respect to the full multivariable controller but it still outperforms the two PI-based closed-loop performance.

Apart from these application specific recommendations, our analysis demonstrated that the improvement of the MIMO controller exists for fundamental and physically motivated reasons. This understanding made the noncontrol engineers involved in this project appreciate the complexity in the model-based control design and support the next phase of experimental validation.

ACKNOWLEDGMENT

The authors would like to thank T. Runolfsson, J. Eborn, C. Haugstetter, and S. Bortoff at the United Technology Research Center for their help and valuable comments.

REFERENCES

- [1] A. Dicks, “Hydrogen generation from natural gas for the fuel cell systems of tomorrow,” *J. Power Sources*, vol. 61, pp. 113–124, 1996.
- [2] S. Ahmed and M. Krumpelt, “Hydrogen from hydrocarbon fuels for fuel cells,” *Int. J. Hydrogen Energy*, vol. 26, pp. 291–301, 2001.
- [3] L. Brown, “A comparative study of fuels for on-board hydrogen production for fuel-cell-powered automobiles,” *Int. J. Hydrogen Energy*, vol. 26, pp. 381–397, 2001.
- [4] V. Recupero, L. Pino, R. Leonardo, M. Lagana, and G. Maggio, “Hydrogen generator, via catalytic partial oxidation of methane for fuel cells,” *J. Power Sources*, vol. 71, pp. 208–214, 1998.
- [5] J. Zhu, D. Zhang, and K. King, “Reforming of CH_4 by partial oxidation: Thermodynamic and kinetic analyzes,” *Fuel*, vol. 80, pp. 899–905, 2001.
- [6] K. Ledjeff-Hey, J. Roses, and R. Wolters, “ CO_2 -scrubbing and methanation as purification system for PEFC,” *J. Power Sources*, vol. 86, pp. 556–561, 2000.
- [7] D. Megede, “Fuel processors for fuel cell vehicles,” *J. Power Sources*, vol. 106, pp. 35–41, 2002.
- [8] L. Pino, V. Recupero, S. Beninati, A. Shukla, M. Hegde, and P. Bera, “Catalytic partial-oxidation of methane on a ceria-supported platinum catalyst for application in fuel cell electric vehicles,” *Appl. Catalysis A: General*, vol. 225, pp. 63–75, 2002.
- [9] T. Springer, R. Rockward, T. Zawodzinski, and S. Gottesfeld, “Model for polymer electrolyte fuel cell operation on reformate feed,” *J. Electrochem. Soc.*, vol. 148, pp. A11–A23, 2001.
- [10] C. Thomas, B. James, F. Lomax Jr, and I. Kuhn Jr, “Fuel options for the fuel cell vehicle: Hydrogen, methanol or gasoline?,” *Int. J. Hydrogen Energy*, vol. 25, pp. 551–567, 2000.
- [11] T. Gardner, D. Berry, K. Lyons, S. Beer, and A. Freed, “Fuel processor integrated H_2S catalytic partial oxidation technology for sulfur removal in fuel cell power plants,” *Fuel*, vol. 81, pp. 2157–2166, 2002.
- [12] A. Larentis, N. de Resende, V. Salim, and J. Pinto, “Modeling and optimization of the combined carbon dioxide reforming and partial oxidation of natural gas,” *Appl. Catalysis*, vol. 215, pp. 211–224, 2001.
- [13] E. Doss, R. Kumar, R. Ahluwalia, and M. Krumpelt, “Fuel processors for automotive fuel cell systems: A parametric analysis,” *J. Power Sources*, vol. 102, pp. 1–15, 2001.
- [14] J. T. Pukrushpan, “Modeling and control of fuel cell systems and fuel processors,” Ph.D. dissertation, Univ. Michigan, Ann Arbor, MI, 2003.
- [15] J. Pukrushpan, A. Stefanopoulou, and S. Varigonda, “Control-oriented model of fuel processor for hydrogen generation in fuel cell applications,” in *Proc. IFAC Symp. Advances in Automotive Control*, Apr. 2004.
- [16] R.-H. Song, C.-S. Kim, and D. Shin, “Effects of flow rate and starvation of reactant gases on the performance of phosphoric acid fuel cells,” *J. Power Sources*, vol. 86, pp. 289–293, 2000.

- [17] J. Eborn, L. Pedersen, C. Haugstetter, and S. Ghosh, "System level dynamic modeling of fuel cell power plants," in *Proc. 2003 Amer. Control Conf.*, pp. 2024–2029.
- [18] S. Scheiber, "Too hot to handle," *Control Eng. Mag.*, vol. 50, no. 6, June 2003.
- [19] *Fuel Cell Handbook*, U.S. Department of Energy, Office of Fossil Energy, and National Energy Technology Laboratory, EG&G Technical Services, Inc, Science Application International Corporation, 2002.
- [20] G. Hunter, R. L. Backford, E. Jansa, D. Makel, C. Liu, Q. Wu, and W. Powers, "Microfabricated hydrogen sensor technology for aerospace and commercial applications," in *Proc. NASA/SPIE Symp.*, San Diego, CA, 1994.
- [21] M. Arcak, H. Gorgun, L. Pedersen, and S. Varigonda, "An adaptive observer design for fuel cell hydrogen estimation," in *Proc. 2003 Amer. Control Conf.*, pp. 2037–2042.
- [22] S. Varigonda, J. Pukrushpan, and A. Stefanopoulou, "Challenges in fuel cell power plant control: The role of system level dynamic models," in *Proc. AIChE Spring Meeting*, 2003, 103b.
- [23] C. de Smet, M. de Croon, R. Berger, G. Marin, and J. Schouten, "Design of adiabatic fixed-bed reactors for the partial oxidation of methane to synthesis gas. Application to production of methanol and hydrogen-for-fuel-cells," *Chem. Eng. Sci.*, vol. 56, pp. 4849–4861, 2001.
- [24] S. Skogestad and I. Postlethwaite, *Multivariable Feedback Control: Analysis and Design*. New York: Wiley, 1996.



Jay T. Pukrushpan received the B.Eng. degree in mechanical engineering from Chulalongkorn University, Bangkok, Thailand, in 1995, the M.S. degree in mechanical engineering from Michigan State University, East Lansing, in 1998, and the Ph.D. degree in mechanical engineering from the University of Michigan, Ann Arbor, in 2003.

He is currently a Faculty Member in the Department of Mechanical Engineering, Kasetsart University, Bangkok, Thailand. His research interests include fuel cell system design, multivariable

control system, hybrid systems, and control design for fuel cell system and fuel processor.



Anna G. Stefanopoulou (S'93–M'96) received the Diploma degree in 1991 from the National Technical University of Athens, Greece, the M.S. degree in naval architecture and marine engineering in 1992 from the University of Michigan, Ann Arbor, and the M.S. and Ph.D. degrees from the Electrical Engineering and Computer Science Department, University of Michigan, in 1994 and 1996, respectively.

She is presently an Associate Professor in the Mechanical Engineering Department at the University of Michigan. She was an Assistant Professor at the University of California, Santa Barbara, and a Technical Specialist at the Ford Research Laboratory.



Subbarao Varigonda (S'99–M'01) was born in Eluru, India. He received the Bachelors degree in chemical engineering from the Indian Institute of Technology, Kanpur, in 1996, the M.S. degree in electrical engineering, and the Ph.D. degree in chemical engineering, both from the University of Minnesota, Minneapolis, in 1999 and 2001, respectively.

He is currently with United Technologies Research Center, East Hartford, CT, where he is working on fuel cell power plant modeling and control design.

His research interests are chemical process modeling, nonlinear dynamics, model based control, control theory and applications.



Lars M. Pedersen (M'00) was born in Copenhagen, Denmark. He received the M.Sc. degree in electrical engineering from Aalborg University, Aalborg, Denmark, in 1990 and the Ph.D. degree in automatic control from the Department of Automatic Control, Lund Technical University, Lund, Sweden, in 1999.

He is currently with United Technologies Research Center, East Hartford, CT, where he is working on modeling and design of vapor compression systems. His research interests are model-based systems design, process control, and applications.



Shubhro Ghosh received the Ph.D. degree in chemical engineering from the California Institute of Technology, Pasadena, in 1994.

He is currently Project Leader in the Fuel Cells Program Office at the United Technologies Research Center (UTRC), East Hartford, CT. His research at UTRC has been primarily on polymer electrolyte membrane (PEM) fuel cells, including systems design, controls, optimization, water management, cold-start, and performance decay.



Huei Peng received the Ph.D. degree in mechanical engineering from the University of California, Berkeley, in 1992.

He is currently an Associate Professor in the Department of Mechanical Engineering, and the Director of Automotive Engineering, University of Michigan, Ann Arbor. His research interests include adaptive control and optimal control, with emphasis on their applications to vehicular and transportation systems.

Dr. Peng has been an active member of SAE and the ASME Dynamic System and Control Division. He has served as the chair of the ASME DSCD Transportation Panel from 1995 to 1997. He is currently an Associate Editor for the IEEE/ASME TRANSACTIONS ON MECHATRONICS. He received the National Science Foundation (NSF) Career award in 1998.